

The 16 April 2015 M_w 6.0 offshore eastern Crete earthquake and its aftershock sequence: implications for local/regional seismotectonics

Ethem Görgün¹ · Kıvanç Kekovalı² · Doğan Kalafat²

Received: 24 March 2016 / Accepted: 1 August 2016 / Published online: 13 August 2016
© Springer-Verlag Berlin Heidelberg 2016

Abstract We examine the 16 April 2015 M_w 6.0 offshore eastern Crete earthquake and its aftershock sequence in southern Aegean Sea. Centroid moment tensors for 45 earthquakes with moment magnitudes (M_w) between 3.3 and 6.0 are determined by applying a waveform inversion method. The mainshock is shallow focus thrust event with a strike-slip component at a depth of 30 km. The seismic moment (M_0) of the mainshock is estimated as 1.33×10^{18} Nm, and rupture duration of the mainshock is 3.5 s. The focal mechanisms of aftershocks are mainly thrust faulting with a strike-slip component. The geometry of the moment tensors ($M_w \geq 3.3$) reveals a thrust-faulting regime with NE–SW-trending direction of T axis in the entire activated region. According to high-resolution hypocenter relocation of the eastern Crete earthquake sequence, one main cluster consisting of 352 events is revealed. The aftershock activity in the observation period between 5 January 2015 and 7 July 2015 extends from N to S direction. Seismic cross sections indicate a complex pattern of the hypocenter distribution with the activation of three segments. The subduction interface is clearly revealed with high-resolution hypocenter relocation and moment tensor solution. The best constrained focal depths indicate that the

aftershock sequence is mainly confined in the upper plate (depth <40 km) and are ranging from about 4.5 to 39 km depth. A stress tensor inversion of focal mechanism data is performed to obtain a more precise picture of the offshore eastern Crete stress field. The stress tensor inversion results indicate a predominant thrust stress regime with a NW–SE-oriented maximum horizontal compressive stress (S_H). According to variance of the stress tensor inversion, to first order, the Crete region is characterized by a homogeneous interplate stress field. We also investigate the Coulomb stress change associated with the mainshock to evaluate any significant enhancement of stresses along Crete and surrounding regions. Positive lobes with stress more than 3 bars are obtained for the mainshock, indicating that these values are large enough to increase the Coulomb stress failure toward NE–SW and NW–SE directions, respectively.

Keywords Aftershock · Coulomb stress analysis · Crete earthquake · Focal mechanism · Moment tensor inversion · Stress tensor inversion

Introduction

The offshore eastern Crete (OEC) earthquake (EQ) sequence occurred at 18:07:44.8 GMT on 16 April 2015. The OEC mainshock was a moderate-size ($M_w = 6.0$) event at a depth of 30 km. The OEC EQ activities are located 50 km offshore eastern part of Crete along the Pliny trench in the Hellenic subduction zone (Fig. 1). The mainshock is revealed by a thrust motion with a minor strike-slip component. The fault rupture zone of the main event extends from 10 to 20 km length due to high-resolution aftershock imaging.

✉ Ethem Görgün
ethem.gorgun@istanbul.edu.tr

Kıvanç Kekovalı
kekovali@boun.edu.tr

Doğan Kalafat
kalafato@boun.edu.tr

¹ Department of Geophysical Engineering, Istanbul University, 34320 Avcılar, Istanbul, Turkey

² Kandilli Observatory and Earthquake Research Institute, Boğaziçi University, 34684 Çengelköy, Istanbul, Turkey

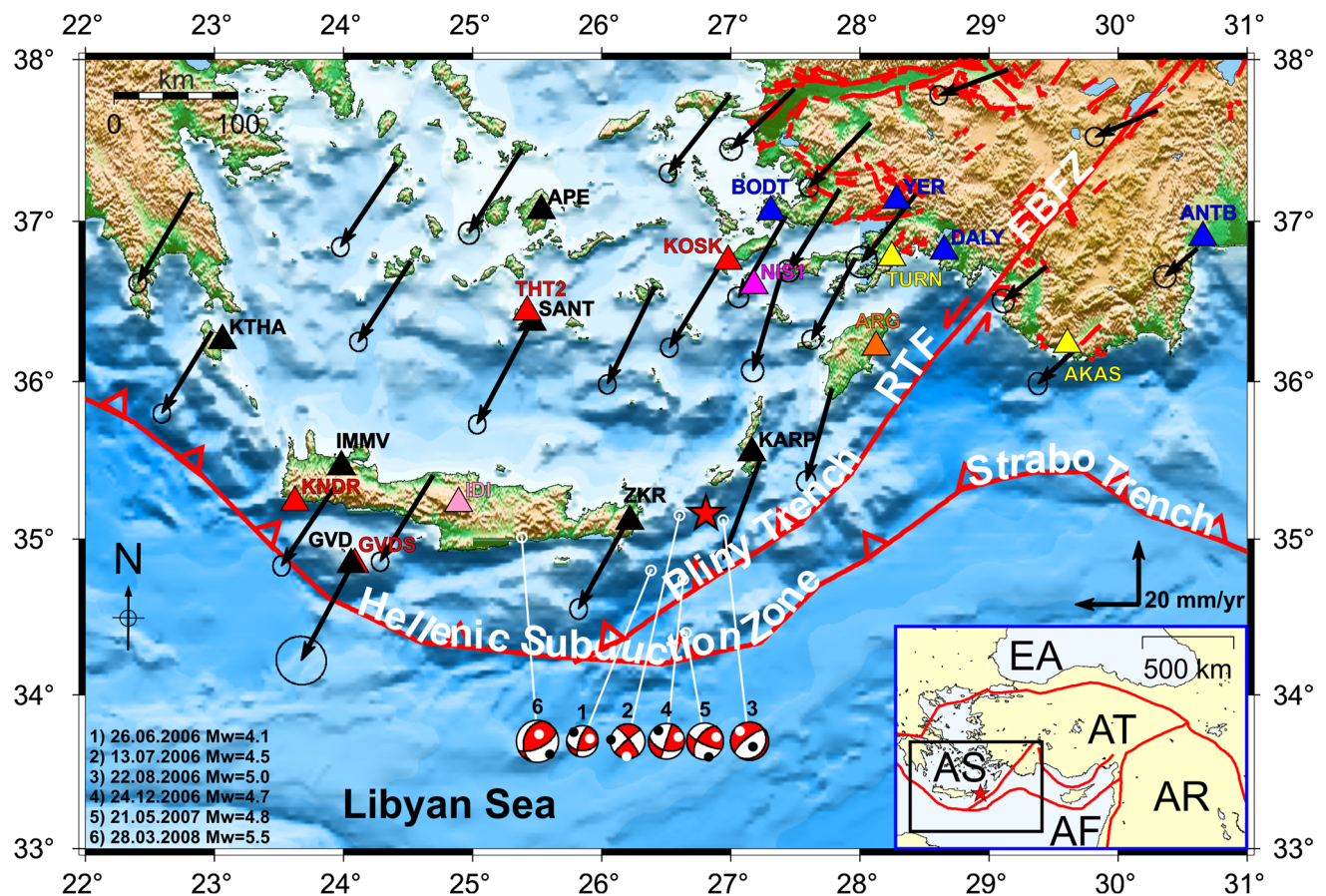


Fig. 1 Tectonic map of southern Aegean Sea showing GPS velocities with respect to Eurasia and 95 % confidence ellipses for western Anatolia (McClusky et al. 2000; Reilinger et al. 2006). Seismically active faults are shown by red lines (Şaroğlu et al. 1992). Blue, black, yellow, purple, orange, red and pink triangles with station codes depict locations of the KOERI, GEOFON, AFAD, THE, NOA, Seismological Network of Crete, MEDNET broadband seismic stations, respectively. The epicenter of the 16 April 2015 eastern Crete mainshock is indicated by the red star. For reference, focal mechanisms of the previous significant earthquakes are plotted (<http://www.emsc-csem.org>). FBFZ and RTF stand for Fethiye–Burdur Fault Zone and

Rhodes Transform Fault, respectively. Two closely spaced red single arrows display shear sense of major faults. Black and white circles on plot of the focal mechanisms exhibit *P* and *T* axes, respectively. The inset in the above right shows whole Turkey. On the lower right-hand corner, a map of the region is shown. Indicated are the boundaries of the plates and microplates in the region. Boundaries (heavy colored red lines) of the Aegean Sea (AS) and Anatolian (AT) plates, which are surrounded by the African (AF), Arabian (AR) and Eurasian (EU) plates (Bird 2003). The solid black rectangle shows the study area, which is enlarged in this figure

The Crete Island is one of the most seismically active parts of the Hellenic subduction zone (HSZ) tectonic regime. The southern Aegean Sea is characterized by very uniform (in magnitude and orientation) plate velocity vectors from Global Positioning System (GPS) indicating SW motion at about 35 mm/year (Fig. 1; McClusky et al. 2000; Reilinger et al. 2006, 2010). It is dominated by a series of thrust and strike-slip structures bounded by normal or oblique faults (McKenzie 1978; Şengör et al. 1985; Mascle et al. 1986; Taymaz et al. 1990, 1991; Taymaz and Price 1992; Le Pichon et al. 1995; Barka et al. 1997; Kreemer and Chamot-Rooke 2004; Skarlatoudis et al. 2009; Le Pichon and Kreemer 2010; Yolsal-Çevikbilen and Taymaz 2012; Yolsal-Çevikbilen et al. 2014; Delph et al. 2015; Fichtner et al. 2013a, b; Vanacore et al. 2013; Kind et al.

2015; Saltogianni et al. 2015). The main seismotectonic structures of the southern Aegean Sea region are the HSZ, Rhodes Transform Fault (RTF), Pliny and Strabo trenches that compose convergent plate boundaries where the African plate (AF) to the south is subducting beneath the Anatolian (AT) and Aegean Sea plates (AS) to the north (inset in Fig. 1). The deformation zone associated with the convergence is very wide from the Peloponnesus to the Strabo trench (Taymaz et al. 1990, 1991; Taymaz and Price 1992; Papazachos 1996; Papazachos et al. 2000; Jost et al. 2002; Skarlatoudis et al. 2009; Yolsal-Çevikbilen and Taymaz 2012; Yolsal-Çevikbilen et al. 2014). Approximately 45° NE trend is observed as an oblique subduction between Pliny trench and HSZ. Compressional motion is transformed into strike-slip on north part of the Pliny trench

and RTF (Fig. 1; Kiratzi and Louvari 2003; Benetatos et al. 2004; Roumelioti et al. 2011; Fichtner et al. 2013a). Crete is located NW of Pliny trench describing the boundary between the AF and AT plates (Fig. 1). Figure 1 indicates an overview on the seismotectonic settings of the Aegean–Anatolian region with the Aegean subduction zone. Crete forms the central part of the HSZ. It is evaluated as a wide thrust fault zone with a large component of strike-slip by well-defined seismicity (Bohnhoff et al. 2005; Becker et al. 2010; Meier et al. 2004; Shaw and Jackson 2010; Yolsal-Çevikbilen and Taymaz 2012; Yolsal-Çevikbilen et al. 2014). Shallow seismicity is observed on the convex side of the HSZ between 0 and 60 km depths (Meier et al. 2004). The crustal structure in Crete is studied using wide aperture seismic data (Bohnhoff et al. 2001), receiver functions and Rayleigh phase velocities (Endrun et al. 2004). Microseismicity and surface wave studies (Meier et al. 2004; Becker et al. 2010) as well as active seismic lines (Bohnhoff et al. 2001) allowed us to improve the structural model along the Aegean subduction zone to illustrate the complex geometry along a strongly curved plate boundary. These studies also display a slab that dips to the North beneath Crete. Endrun et al. (2004) indicate that the average depth of the subducted oceanic Moho is 55 km beneath Crete. On the basis of S receiver functions, the lithosphere–asthenosphere boundary of the subducting AF is at 100 km depth beneath the southwestern part of Anatolia and dips beneath the volcanic arc to a depth of about 225 km and therefore implies a thickness of 60–65 km for the subducted African lithosphere (Soudoudi et al. 2006; Fichtner et al. 2013a, b; Vanacore et al. 2013; Kind et al. 2015).

The epicenter distribution of recent moderate-size earthquakes ($M_w \geq 4.0$) that have occurred since 2006 around the offshore eastern Crete is shown in Fig. 1. The distribution of these epicenters indicates a very low activity compared with north or south of Crete (Becker et al. 2010). These earthquakes are mostly upper plate events (depth ≤ 60 km) (Becker et al. 2010). The seismic pattern of Crete and surrounding area is generally characterized by moderate-size events. The focal mechanisms of these important recent events are displayed at the lower part of Fig. 1. Among them, the 26 June 2006 ($M_w = 4.1$), 13 July 2006 ($M_w = 4.5$), 22 August 2006 ($M_w = 5.0$) and 24 December 2006 ($M_w = 4.7$) are significant events that can be related to the OEC EQ thrust and strike-slip system combination. These recent events indicate a complex thrust/strike-slip fault zone, which has also a normal faulting event (#3 EQ, see Fig. 1). We interpret their orientation and spatial distribution in terms of the major thrust/strike-slip fault strands and the basin boundaries (for the normal faults).

In this study, we performed a stress tensor inversion from earthquake focal mechanisms to obtain a more accurate

picture of the OEC EQ stress field. For this purpose, seismic waveforms at local and regional distances were used to calculate source parameters of 45 events ($3.3 \leq M_w \leq 6.0$) of the OEC M_w 6.0 EQ sequence using the waveform inversion method (Nakano et al. 2008). This provides additional information on the stress field that is able to improve kinematic models for Crete and thus develop the understanding of the local and regional tectonics. Furthermore, the double-difference relocation algorithm (Waldhauser and Ellsworth 2000) and the Coulomb stress analysis (Toda et al. 2011) were applied to determine the expanded spatial distribution of the OEC EQ sequence. Determination of accurate source parameters, especially source locations, using data from the local and regional seismic networks is crucial for investigations of the seismotectonics in and around southern Aegean Sea.

Data and waveform inversion method

Figure 1 displays the distribution of the Kandilli Observatory and Earthquake Research Institute (KOERI, 4 stations), GeoForschungsZentrum Potsdam GEOFON (GFZ, 7 stations), Disaster and Emergency Management Presidency Earthquake Department (AFAD, 2 stations), Aristotle University of Thessaloniki Seismological Network (THE, 1 station), National Observatory of Athens (NOA, 1 station), Seismological Network of Crete (SNC, 4 stations) and MEDNET (1 station) broadband seismic stations used in this study.

We computed centroid moment tensor (CMT) solutions of earthquakes in the eastern Crete using the waveform inversion method developed by Nakano et al. (2008). In this approach, if the location yielding a minimum residual lies at the edge of a search area, the grid is extended to surround the location of the minimum residual. When the location of minimum residual lies within a search area, a new search was performed around the location using a reduced grid spacing to find a detailed source location. The seismic moment and rupture duration were estimated from the deconvolved form of the moment function (Nakano et al. 2008, 2010).

We used three-component broadband seismograms for the inversion of the OEC EQ sequence. Seismograms with good data quality were selected. The average number of waveforms used for the CMT analysis is 10. The observed velocity seismograms were corrected for instrument response and then integrated in time to obtain the displacement seismograms. Waveforms were band-pass-filtered between 20 and 50 s and decimated to a sampling frequency of 0.5 Hz. A total data length of 512 s (256 data points in each channel) was used for the inversion. Green's functions were generated using the discrete wavenumber

method (Bouchon 1979), assuming the crustal structure model of Becker et al. (2010) for the calculation. Green's functions were computed for every 10 km of epicentral distance up to 1500 km. At each of these radius steps, three-component displacements were calculated at every 1° in azimuth for each basis of moment tensor. Green's functions were calculated at every 5 km for source depths shallower than 100 km. For spatial grid search, hypocenter locations estimated by KOERI were used as an initial location. Adaptive grid spacings, in which the grid spacings are gradually decreased in each step of the search, are also applied. Spatial grid search was started with a horizontal grid spacing of 0.5° and a vertical grid spacing of 10 km. In the next step, the grid spacing was reduced to 0.2° horizontally and 5 km vertically. Finally, the horizontal grid spacing was reduced to 0.1°. At each grid point, the fault and slip orientation parameters (strike, dip and rake angles) were searched in 5° steps. For each combination of source location, fault and slip orientation parameters, the waveform inversion was carried out to estimate the best-fitting source parameters (see Nakano et al. 2008, 2010 for details).

The CMT solutions were obtained using data not only from stations in Greece but also from Turkey, and therefore, azimuthal coverage was sufficient. The inversion method of Nakano et al. (2008) used the double-couple constraint, which stabilizes the inversion solution and reduces the trade-off between source location and non-double-couple components (see Nakano et al. 2008, for details). Furthermore, all stations used are located in Anatolia, Crete, Dodecanese Islands and Cyclades; thus, possible effects of the structural contrast may be minimized. Determination of accurate source parameters, especially source locations, using data from the local and regional seismic network is crucial for investigations of the seismotectonics in and around Turkey and Greece.

Stress tensor inversion

The stress tensor has six unknowns, either three principal stresses and orientations, or three normal and three shear stress components (e.g., Zang and Stephansson 2010). Four of the unknowns are resolved by the inversion of the stress tensor, the fifth unknown is calculated by the assumption that slip occurs in the direction of maximum shear stress (Wallace 1951; Bott 1959) and the sixth unknown is usually resolved using the assumption that the stress tensor is homogeneous and constant in the binning region throughout the time interval of interest.

In this study, we apply the technique of Michael (1984, 1987) to the selected 45 events. The Michael approach provides a more appropriate estimate of uncertainty, compared to Gephart and Forsyth (1984) approach (Hardebeck and

Hauksson 2001). The algorithm uses the statistical method of bootstrap re-sampling and allows determining the orientation of the three principal stresses (σ_1 = maximum principal compressive stress, σ_2 = intermediate and σ_3 = minimum) as well as the stress ratio $\phi = (\sigma_2 - \sigma_3)/(\sigma_1 - \sigma_3)$, also called relative stress magnitude (Bott 1959). The ϕ is defined using the standard geologic/geophysical notation with compressive stress positive and $\sigma_1 > \sigma_2 > \sigma_3$ (Zoback 1992). The stress ratio ϕ ranges from 0 to 1. Values of $\phi < 0.5$ and $\phi > 0.5$ indicate a transpressional and transtensional regime, respectively. All parameters are determined by finding the best-fitting stress tensor to the observed focal mechanisms. Assumptions that must be fulfilled by the input data are: (1) stress is uniform in the area of interest during the observed time interval; however, this assumption cannot be entirely valid given the diversity and complexity of the structures, (2) earthquakes are shear dislocations on preexisting faults, (3) similar shear stress magnitude are present on each fault and (4) slip occurs in the direction of the resolved shear stress on the fault plane.

To quantify the misfit between the best stress tensor and the data, the angle between the calculated slip vector from stress tensor inversion and observed slip vector from fault plane solutions is used. This angle is referred to as β . The angle $\bar{\beta}$ refers to the mean value of β for the data in a single inversion (Michael 1987). A synthetic control study showed that the amount of heterogeneity in the stress field could be characterized by the average misfit between the observed and predicted slip directions ($\bar{\beta}$) (Michael et al. 1990). If $\bar{\beta} \leq 33^\circ$, stress tensors are spatially uniform. If $\bar{\beta} > 33^\circ$, the inversion result is interpreted in terms of a spatially heterogeneous state of stress (Michael 1991). Heterogeneity of the stress field was documented in the average misfit level of the inversion. For each stress inversion, 2000 bootstrap iterations are performed.

Michael's algorithm is quite fast and accurate when compensating the directions of the principal stresses. It gives a reasonable accuracy even for randomly selected fault planes in focal mechanisms. However, the accuracy of the stress ratio is significantly lowered when the fault planes are not correctly chosen. The stress ratio is more sensitive to the correct choice of the fault plane than the principal stress directions, and substituting the faults by the auxiliary nodal planes introduces high errors (Lund and Slunga 1999; Vavryčuk 2014). This difficulty is removed by modifying Michael's algorithm and inverting jointly for stress and for fault orientations (Vavryčuk 2014). The fault orientations are determined by applying the fault instability constraint, and the stress is calculated in iterations. As a by-product, overall friction on faults is determined. Vavryčuk (2014) showed that the new iterative stress inversion is fast and accurate and performs much better than the standard linear inversion. Since the iterative stress inversion is based

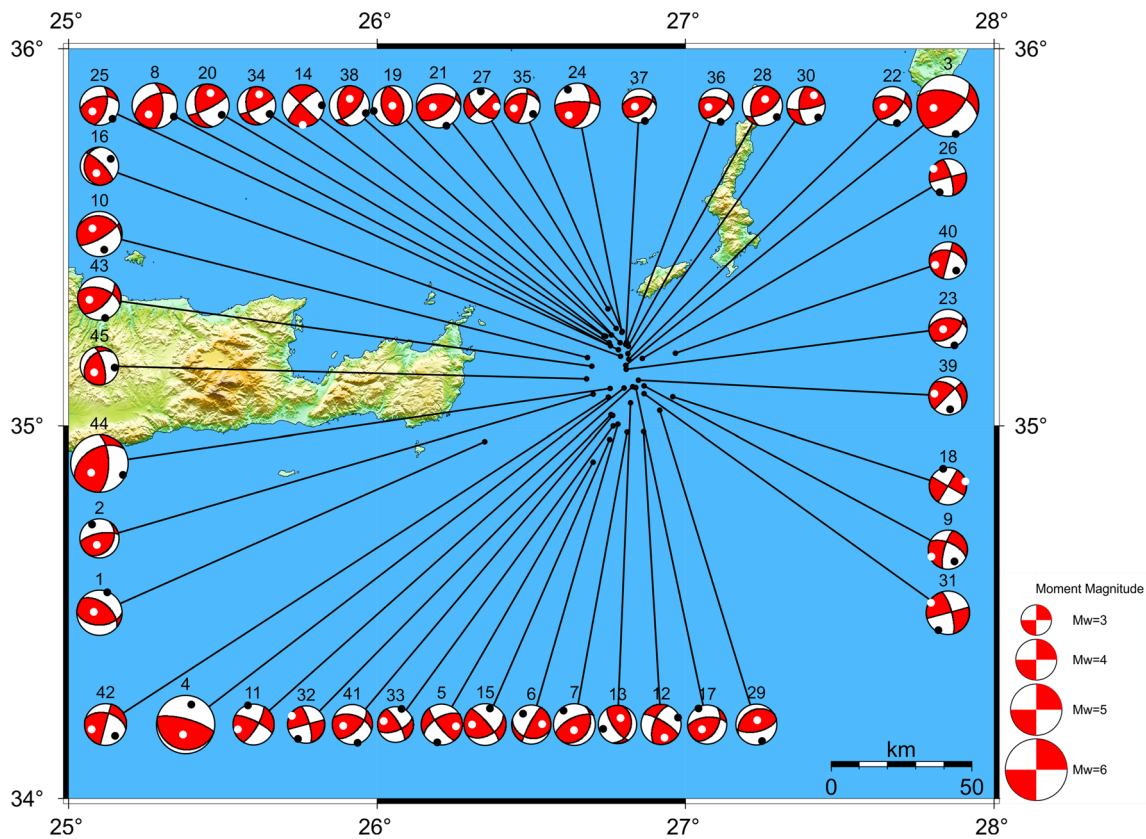


Fig. 2 Topographic map view of CMT solutions obtained by the waveform inversion method developed by Nakano et al. (2008). Focal mechanisms are projected on the lower hemisphere and scaled with

magnitude. *Black and white circles* on plot of the focal mechanisms exhibit *P* and *T* axes, respectively

on Michael’s method, it can easily be implemented in these codes enhancing their accuracy. Vavryčuk (2014) proposed the MATLAB code of this inversion called STRESSINVERSE is provided on the Web page (<http://www.ig.cas.cz/stress-inverse>).

Results

From the spatial distribution of the CMT solutions (Fig. 2), we observe a prominent N–S alignment of nodal planes. The along-strike dimension of the activated zone is ~70 km, and its width is approximately 18 km. The moment magnitudes (M_w) range from 3.3 to 6.0. Figures 2 and 3 display 45 fault plane solutions in lower-hemisphere equal-area/angle projection in map view and cross section (profile A–A’), respectively.

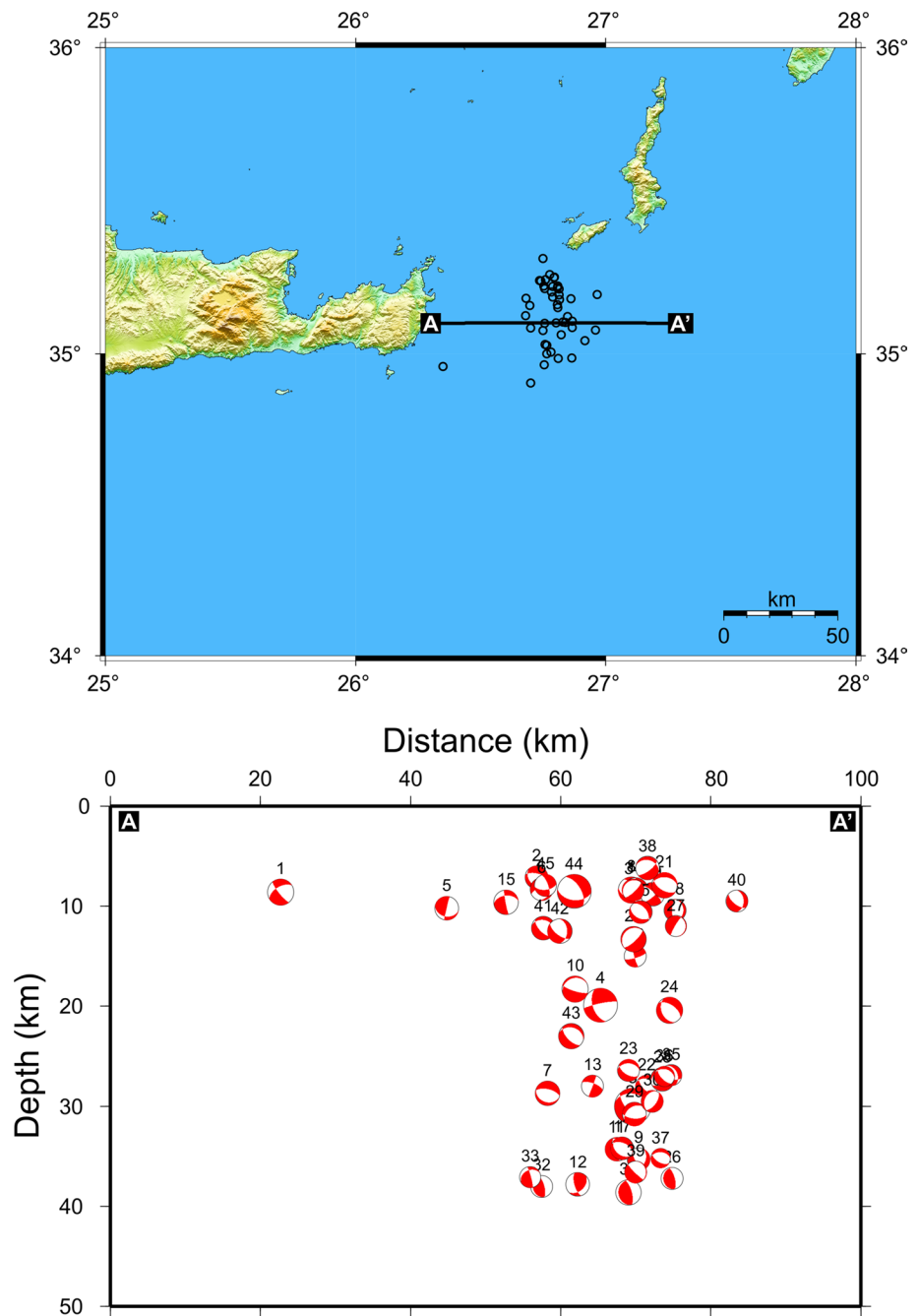
The 16 April 2015 M_w 6.0 offshore eastern Crete mainshock

In this section, we present the mainshock ($M_w = 6.0$) of the OEC EQ sequence. The largest event of the EQ sequence

is chosen as an example. It would be interesting to present this large-size event whose focal mechanism differs from some of the aftershocks. This event is representative of the data set. The results of the 45 selected events are given in Table 1.

First, we estimate the source centroid location and focal mechanism of the 16 April 2015 M_w 6.0 event. Waveforms recorded by six stations (APE, ARG, GVD, IDI, IMMV and TURN; Fig. 4, blue triangles), which are located at epicentral distances ranging from approximately 160 to 270 km, are used. Figure 4 shows the horizontal residual distribution around the best-fitting source location obtained from the waveform inversion. The best-fitting source location is at 26.806°E, 35.161°N at a depth of 30 km (Fig. 4). Using the hypocenter location determined by KOERI as an initial source location, the waveform inversion searched for the best-fitting source parameters. Revised source locations vary in average 4 km horizontally and 5 km vertically with respect to the initial locations of KOERI, but this variation does not change the general pattern in seismicity. Location differences depend on velocity model, station coverage and number of stations participated in finding the hypocenter. The observed velocity waveforms are corrected for

Fig. 3 Epicenter distribution of the selected aftershocks ($M_w \geq 3.3$) in the region offshore eastern Crete. A–A' is the depth cross-sectional profile. Cross section is perpendicular to the strike of the fault rupture. This is a zooming for the narrower region along the mainshock area. The aftershock sequence lies in the depth range from 5 to 40 km for $M_w \geq 3.3$ events. Orientation of aftershocks trends NW–SE. The main aftershock cluster is clearly depicted in the ~25 km width vertical zone of the cross section



instrument response, and then, they are integrated in time to obtain the displacement seismograms. The focal mechanism of the mainshock obtained at the best-fitting source location is related to thrust faulting with minor strike-slip component (Fig. 5), characterized by a nodal plane with strike, dip and rake 288° , 52° and 141° , respectively. The seismic moment of the event is estimated as $M_o = 1.33 \times 10^{18}$ Nm, and the corresponding moment magnitude is $M_w = 6.0$. Waveform fits between observed and synthetic seismograms calculated

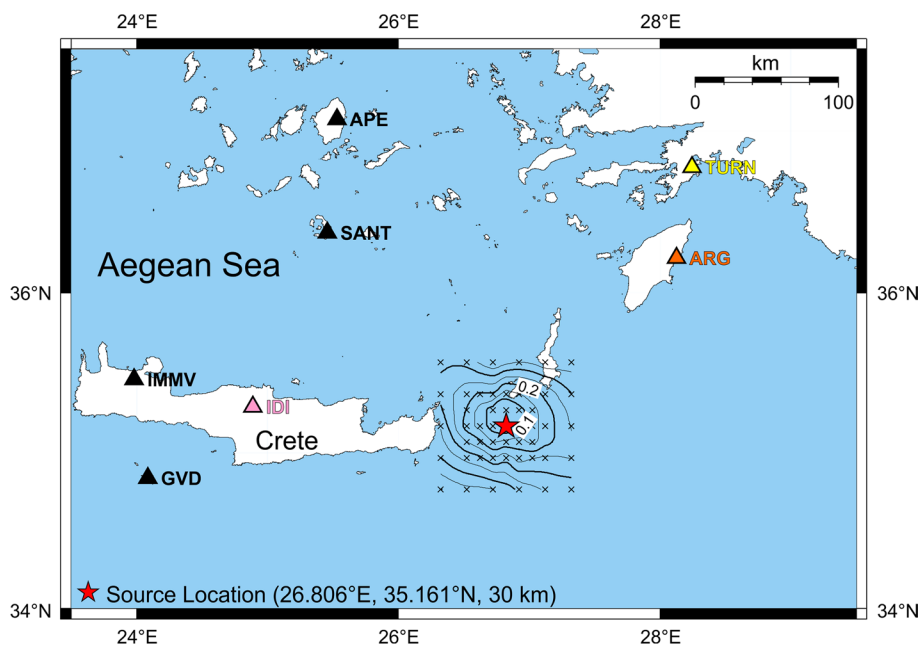
for the best-fitting source parameters are shown in Fig. 5 (Nakano et al. 2008 for details on the approach). Waveform fits are in good agreement with a normalized residual (R) of 0.06 (Fig. 5). The residuals are calculated for each focal mechanism solution in this study (Table 1). The seismic moment function for the mainshock obtained from the waveform inversion is shown in Fig. 5. The rupture duration of the 16 April 2016 OEC EQ estimated from the moment function is 3.5 s (upper right in Fig. 5).

Table 1 Locations and source parameters of the 16 April 2016 eastern Crete earthquake sequence

No	Date	Time (GMT)	Lat (°N)	Lon (°E)	<i>H</i> (km)	M_w	Str (°)	Dip (°)	Rake (°)	<i>R</i>
1	05.01.2015	11:53:58.91	34.9578	26.3490	8.6	4.4	90	45	60	0.08
2	17.01.2015	01:59:41.56	35.0842	26.7005	7.1	3.8	30	30	45	0.06
3	16.04.2015	18:07:44.80	35.1610	26.8060	30	6.0	288	52	141	0.06
4	17.04.2015	02:05:41.95	35.1015	26.8012	19.9	5.7	285	75	90	0.07
5	17.04.2015	07:50:30.60	34.9035	26.7002	10.2	4.0	240	60	15	0.09
6	17.04.2015	08:35:45.85	35.0048	26.7815	8.3	3.8	208	83	61	0.05
7	17.04.2015	10:23:43.49	34.9842	26.8105	28.7	4.1	244	64	106	0.11
8	17.04.2015	11:30:37.58	35.2135	26.7563	8.4	4.4	243	52	141	0.04
9	17.04.2015	16:34:10.94	35.1070	26.8660	35.3	3.8	195	75	−30	0.06
10	17.04.2015	16:39:44.82	35.1823	26.6822	18.3	4.4	286	21	134	0.08
11	18.04.2015	03:59:31.94	35.1040	26.8290	34.3	4.0	30	75	15	0.10
12	18.04.2015	13:42:10.84	34.9852	26.8643	37.8	3.9	202	61	163	0.09
13	18.04.2015	15:31:13.98	35.0620	26.8220	28	3.7	15	30	135	0.06
14	19.04.2015	02:48:47.79	35.2390	26.7412	8.4	4.1	225	75	180	0.07
15	19.04.2015	06:35:01.14	34.9638	26.7537	9.6	4.1	60	45	15	0.12
16	19.04.2015	14:20:03.48	35.1858	26.7888	15	3.7	315	75	75	0.09
17	19.04.2015	21:42:26.50	35.1025	26.8393	34.2	3.8	265	60	125	0.11
18	19.04.2015	22:21:36.94	35.0773	26.9585	10.4	3.6	30	90	0	0.04
19	19.04.2015	23:36:48.52	35.2213	26.7885	8.8	3.9	345	45	90	0.06
20	20.04.2015	07:43:03.26	35.2220	26.7527	13.3	4.2	64	79	134	0.09
21	21.04.2015	01:57:39.73	35.2593	26.7757	7.9	4.3	270	45	120	0.14
22	21.04.2015	02:45:57.82	35.1780	26.8160	28	3.7	288	52	141	0.05
23	21.04.2015	07:18:36.63	35.1512	26.8077	26.4	3.7	270	45	120	0.12
24	22.04.2015	20:19:55.80	35.2498	26.7933	20.4	4.4	15	47	21	0.09
25	22.04.2015	22:17:35.12	35.2033	26.7825	10.6	3.8	258	52	141	0.15
26	24.04.2015	04:08:36.35	35.1803	26.8603	37.2	3.6	255	90	−15	0.12
27	27.04.2015	08:24:05.93	35.3123	26.7485	12	3.5	225	90	30	0.09
28	27.04.2015	14:16:32.08	35.2125	26.8142	27.3	3.9	60	60	120	0.11
29	03.05.2015	16:46:18.89	35.0422	26.9162	30.8	4.0	240	30	75	0.15
30	05.05.2015	13:31:27.64	35.1928	26.8133	29.5	3.7	82	77	149	0.09
31	11.05.2015	05:02:00.81	35.0863	26.8658	38.6	4.2	255	90	−15	0.05
32	11.05.2015	18:10:15.80	35.0307	26.7578	38	3.6	255	90	−15	0.08
33	11.05.2015	18:14:48.68	34.9997	26.7653	37.1	3.5	68	61	17	0.08
34	16.05.2015	18:43:16.58	35.2398	26.7357	8.4	3.7	64	79	134	0.12
35	21.05.2015	00:03:04.75	35.2515	26.7950	26.9	3.5	261	33	152	0.11
36	21.05.2015	00:11:53.89	35.2225	26.8088	27	3.4	288	52	141	0.06
37	21.05.2015	00:41:33.93	35.2168	26.8067	35.2	3.3	270	45	120	0.03
38	22.05.2015	22:09:19.00	35.2427	26.7595	6.2	3.9	45	60	120	0.05
39	24.05.2015	09:57:56.90	35.1218	26.8470	36.6	3.7	225	90	−45	0.08
40	28.05.2015	00:33:03.23	35.1937	26.9667	9.5	3.6	195	90	−45	0.09
41	28.05.2015	12:56:38.56	35.0273	26.7640	12.2	3.9	288	52	141	0.06
42	28.05.2015	12:59:24.26	35.0767	26.7493	12.5	4.1	195	90	−45	0.11
43	29.05.2015	00:03:50.40	35.1588	26.6963	23	4.2	288	52	141	0.05
44	09.06.2015	21:49:47.08	35.0993	26.7555	8.5	5.6	240	45	141	0.07
45	15.06.2015	04:15:58.68	35.1255	26.6792	7.9	3.7	225	35	145	0.08

H is depth, M_w is moment magnitude, *Str* is strike angle and *R* is the normalized residual of waveform fitting ($R = 0$ would mean a perfect fit and $R = 1$ no fit at all)

Fig. 4 Map showing the source centroid locations and contour plots of the horizontal residual distribution around the best-fitting source (*red star*). *Black, yellow, orange and pink triangles* with station codes indicate locations of the GEOFON, AFAD, NOA and MEDNET broadband stations, respectively. The *red star* indicates 16 April 2015 $M_w = 6.0$ mainshock



Relocation of hypocenters

We select 470 events that are well recorded by at least three stations for six-month period following the date of 5 January 2015. We calculate the absolute hypocentral parameters of aftershocks with the hypocenter location algorithm described by Lienert and Havskov (1995). In general, we locate all earthquakes using the 1-D (P- and S-wave) velocity model of Becker et al. (2010). We choose only events with at least 4 P-phases and 1 S-phase, hypocenter parameters with RMS errors < 0.5 s, azimuthal gap $< 180^\circ$ and horizontal and vertical errors < 1 km, using the HYPOCENTER earthquake location program (Lienert and Havskov 1995). The catalog covers the period from 16 April 2015 to 7 July 2015 for shallow earthquakes with hypocentral depth < 40 km. Figure 6 shows the epicentral and hypocentral distributions in the eastern Crete region. The catalog consists of 470 events. The average horizontal and vertical uncertainties of the 470 events ($M_1 \geq 1.4$) are found to be 3 and 4 km, respectively. In minimizing the errors in the location parameters, network geometry, phase reading quality and uncertainties in the crustal structure are restricting factors. Relative earthquake location methods can improve absolute hypocenter locations. For this purpose, the double-difference relocation algorithm (HypoDD, Waldhauser and Ellsworth 2000) is used. The algorithm assumes that the difference in travel times for two close events observed at one station can be connected to the spatial offset between the events with high accuracy. Absolute location parameters of aftershocks and P/S travel time differences between the event pairs are used for the inputs. Event locations are improved for the 6-month period that

the aftershock sequence mainly operated. Relative location errors of the 352 relocated events are smaller than 1 km in horizontal and vertical directions.

The main EQ cluster consisting of 352 events is located offshore Crete. The aftershock activity in the observation period between 16 April 2015 and 7 July 2015 extends from the north to the south direction (Fig. 6). This observation is also shown in the cross section inclined to the fault rupture (Fig. 6, profile B–B', red). The best constrained focal depths (from waveform modeling and hypoDD analysis) indicate that the aftershock sequence is mainly confined in the upper crust (depth < 40 km) and is ranging from 4.5 to 39 km. The main aftershock cluster (Fig. 6, profiles B–B', C–C' and D–D') is clearly depicted with a 30-km vertical extension in all three cross sections.

In the northernmost end of the main cluster, the seismicity occurred in a zone extending about 18 km east to west and the depths of the aftershocks are found to be between 4.5 and 38 km (Fig. 6, profile B–B', by red). The middle of the main cluster (profile C–C', orange) covers aftershocks occurring at depths of 5 and 39 km. The dip angle of the NW–SE nodal plane (Fig. 5, top left) complies with the alignment of the aftershocks on the C–C' cross section in Fig. 6. This observation does not contradict the results of the cross section perpendicular to the fault rupture (Fig. 3, profile A–A'). The southernmost end of the main cluster (profile D–D', purple in Fig. 6) is associated with a fault plane trending mainly NW–SE direction.

Figure 7a, b shows the frequency of analyzed events with respect to the computed M_1 and hypocentral depth. We observe that most of events lie in the M_1 range from 2.5 to 3.5. In addition to this, depth ranges mainly from 5 to

15 km. Most events occur in the depth range between 5 and 15 km. The seismicity decreases nearly to zero in the depth range between 15 and 18 km. The number of events slowly increases with increasing depth from 18 to 25 km. In the depth range of 25–38 km, a relative maximum of events occur. In the depth range of 15–25 km, the amount of brittle fracture is significantly reduced. Figure 7c indicates cumulative number of EQ as a function of time.

Analysis of stress tensors

The results of the stress tensor inversion are presented in Fig. 8 and Table 2. The measure of the misfit values is evaluated by the areas of 95 % confidence limit (see Fig. 8). Stress tensor inversion of the OEC EQ aftershocks reveals a heterogeneous stress for the entire catalog ($\beta = 44^\circ$) according to Michael (1991). The maximum principal stress, σ_1 , trends S153°E with a plunge of 4° , and the minimum principal stress, σ_3 , trends S250°W with a plunge of 64° (Fig. 8b). The resulting stress tensor corresponds to a transtensional regime ($\phi = 0.60$, Fig. 8c). The orientation of maximum horizontal compressive stress (S_H) is NW–SE, and thrust stress regime is found for the study region.

High variance (0.18, Table 2) indicates heterogeneous stress tensor from the observed focal mechanisms and correlates with a large heterogeneity of the stress field (Michael et al. 1990; Lu et al. 1997; Wiemer et al. 2002; Bohnhoff et al. 2006; Görgün et al. 2010). The alignment of σ_1 is NW–SE. Deformation regimes obtained from the stress tensor inversion indicate the predominant thrust stress regime along the area of Crete. We conclude that a high degree of heterogeneity in stress field with high variance indicates heterogeneity. There is a significant variance in stress tensor orientations. Thus, the Crete region is characterized by a heterogeneous interplate stress field.

Calculation of the Coulomb stress change

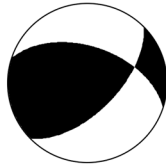
The static Coulomb stress change caused by a mainshock has been widely applied to assess areas of subsequent off-fault aftershocks (Reasenber and Simpson 1992; Toda et al. 2008, 2011). The Coulomb stress change is defined as $\Delta CFF = \Delta\tau + \mu\Delta\sigma$, where τ is the shear stress on the fault (positive in the inferred direction of slip), σ is the normal stress (positive for fault unclamping) and μ is the apparent friction coefficient. Failure is promoted if ΔCFF is positive and inhibited if negative; both increased shear and unclamping of faults are taken to promote failure, with the influence of unclamping controlled by fault friction (Toda et al. 2011). After the occurrence of an earthquake, the areas with positive values of ΔCFF are loaded with stress. The Coulomb stress change on a ‘receiver fault’ (fault receiving stress from a mainshock) requires a source

model of the earthquake fault slip, as well as the geometry and slip direction on the receiver (Toda et al. 2011). It is assumed that the receiver faults share the same strike, dip and rake as the mainshock source fault, and we can resolve stress on a major fault of known geometry (McCloskey et al. 2003). We can also find the receiver faults at every point that maximize the Coulomb stress increase given the earthquake stress change and the tectonic stress (King et al. 1994), termed the ‘optimally oriented’ Coulomb stress change (Toda et al. 2011).

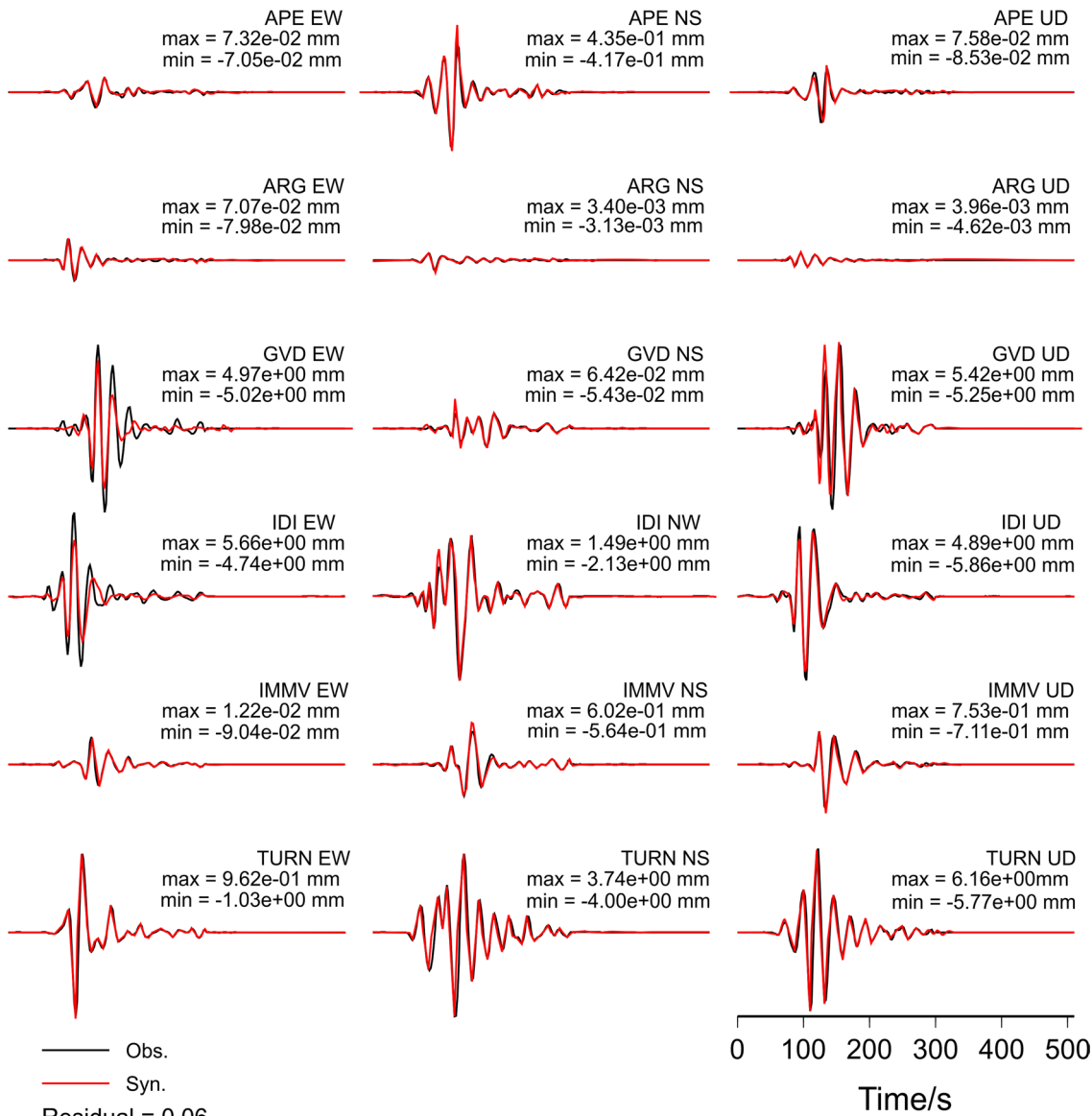
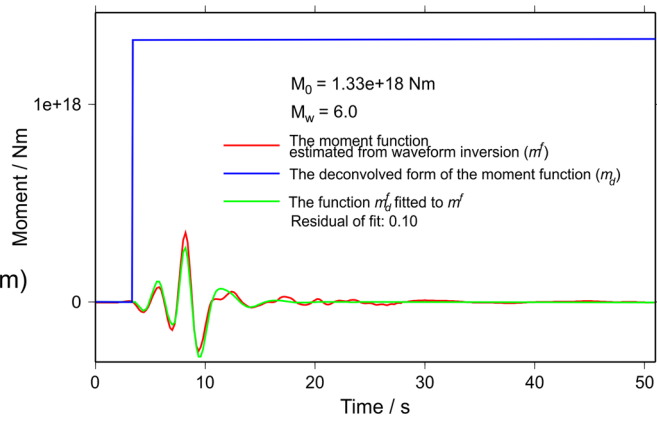
We used the mainshock (M_w 6.0) source parameters deduced from waveform modeling to calculate the Coulomb stress change (Table 1). The principal axes of the stress tensor were also used to compute the spatial distribution of the Coulomb stress change (Table 2). The stress changes are resolved at 45 km depth based on the estimated geometry of major active faults. Increased shear stress in the rake direction and unclamping on surrounding ‘receiver’ faults are interpreted to promote failure (Toda et al. 2008). The Coulomb 3.3 software (www.coulomb-stress.org) is used to project thrust-faulting mechanism at a depth of 45 km with a strike/dip/rake of $288^\circ/52^\circ/141^\circ$ and a friction coefficient $\mu = 0.4$ in an elastic half space with uniform isotropic elastic properties (Lin and Stein 2004; Toda et al. 2005, 2008, 2011).

The spatial distribution of the Coulomb stress change due to the occurrence of the 16 April 2015 M_w 6.0 OEC EQ is presented in Fig. 9. Stress increase regions close to failure are represented by the red lobes. Positive Coulomb stress change is observed in NW–SE and NE–SW directions of the rupture zone. The eastern and western ends of the OEC EQ rupture are brought to 3–5 bars closer to failure. Stress changes of ≥ 0.1 bars are generally observed to influence seismicity rates (King et al. 1994).

To further compare the Coulomb stress change and aftershocks, a cross section is presented in Fig. 10 along the profile A–B shown in Fig. 9. Here, the stress is resolved on the dominant focal mechanism, which in most cases is thrust faulting. We find that the spatial and depth distribution of aftershocks and their focal mechanisms are consistent with the calculated Coulomb stress changes imparted by the coseismic rupture. Most of the aftershocks lie in the OEC EQ region (Fig. 10) for which the Coulomb stress decreased (mainshock energy released) by ≤ -5 bars, and there is a stress drop between 10 and 50 km depths (Fig. 10). Nevertheless, many aftershocks (especially upper crust <15 km events) are located far from the fault plane, where the positive Coulomb stress change is out of range. These earthquakes may only be consistent with stress transfer if they strike on faults with different orientations, such as secondary strike-slip or oblique focal mechanism as shown in Figs. 2 and 3. Taking into account the mainshock and its aftershocks, the dimension of the activated



(strike, dip, rake) = (288°, 52°, 141°)
 (lon, lat, depth) = (26.806°, 35.161°, 30 km)
 $M_0 = 1.33e+18$ Nm, $M_w = 6.0$



Residual = 0.06
 Frequency range
 0.02 - 0.05 (Hz)

Fig. 5 Estimated focal mechanism and source parameters of the event. Waveform fittings obtained from the waveform inversion. *Black and red lines* represent the observed and synthesized seismograms, respectively. The station code and component of motions are indicated at the upper right of each seismogram. Maximum and minimum displacements are shown at the upper right of each seismogram. *Upper right side*, the moment functions (m' , *red line*) and the functions m'_d (*green line*) obtained from the waveform inversion of the 16 April 2015 M_w 6.0 mainshock. *Blue line* represents the deconvolved form of the moment function (m_d)

area can be explained on the basis of the Coulomb failure criterion because of stress transfer loading. In this way, the post-seismic stress changes affect the production of aftershocks, as evaluated by spatial and depth distributions of focal mechanisms.

Discussion

The spatiotemporal and source characteristics of the 16 April 2015 M_w 6.0 OEC EQ sequence are investigated. The distribution of relative relocated hypocenters and focal mechanisms clearly indicates the activation of a S153°E-trending thrust fault system offshore eastern Crete region. The stress tensor inversion results reveal a predominant thrust stress regime with a NW–SE-oriented maximum horizontal compressive stress (S_H). The entire study region is rather heterogeneous according to the stress tensor inversion variance (0.18). The relative stress magnitude (stress ratio, ϕ) is estimated to be 0.60 (transtensional stress regime) for the OEC EQ region. Therefore, the region offshore eastern Crete is characterized by a heterogeneous interplate stress field as far as the orientation of stress is concerned (Fig. 8).

The aftershocks source mechanisms are dominantly thrust motion with T axis-oriented NE–SW. The source centroid depths reveal that these earthquakes occurred along a fault located in the shallow crust. The T axis orientations in the EC aftershocks are consistent with the GPS observations (McClusky et al. 2000; Nyst and Thatcher 2004; Le Pichon and Kreemer 2010; Reilinger et al. 2010). GPS vectors display an SSW-oriented strike-slip movement as the primary source of the mainshock (McClusky et al. 2000; Reilinger et al. 2010; Fig. 1). The focal mechanism solutions of the OEC EQ and the high-resolution aftershock locations suggest that we interpret their orientation and spatial distribution in terms of the major thrust fault strands and the basin boundaries (for the normal faults). Focal mechanisms display not only thrust mechanisms but also strike-slip mechanisms. These strike-slip or oblique mechanisms may occur due to the local stress change in the activated region after the mainshock. Moreover, the aftershocks in southern part of the mainshock show that several

small fault segments exist in this area. These small secondary faults may have different faulting mechanisms with the main cluster (i.e., events 32 and 33, Table 1).

In the area of Crete, the structure of the upper 20 km is defined by results of wide-angle seismic reflections (Bohnhoff et al. 2001). The thickness of the upper crust of the AS plate is well determined and ranges from 8 to 13 km beneath Crete. Receiver function (Knapmeyer and Harjes 2000; Endrun et al. 2004) and surface wave studies (Meier et al. 2004) display that the average depth of the oceanic Moho within the NE-dipping subducting African lithosphere is about 55 km below Crete. In this study, high-resolution hypocenter determinations are projected onto the profiles shown in Fig. 6. Along profiles B–B', C–C' and D–D', the epicentral distance to each profile does not exceed 20 km. On profiles B–B', C–C' and D–D', hypocenters cluster along the interface or contact between the plates. The lateral width of the seismogenic zone is about 25 km. The interface between the AS and AF plates is seismically active where the interface is located between about 5 and 40 km depths. At shallower depth (<15 km), plenty of events are detected around the interface. There is an offset between 15 and 23 km depths. On profile D–D', this offset is approximately 10 km wide. It might be interpreted as decollement, as in this region, the relative motion of the plates caused mainly ductile deformation during the time of observation (Meier et al. 2004; Becker et al. 2010). Interplate seismicity within the HSZ and Pliny trench indicates a seismically active NW-dipping zone. Below 15 km depth, this zone appears to be almost parallel to the interface between the plates. At depth greater than 20 km below Crete, seismicity is gradually reduced in the AS plate. The concentration of seismicity along the Pliny trench extends from shallow depths down to the plate interface and indicates active movement. The crustal seismicity of the AS plate in this area is generally confined to the upper 20 km in agreement with the idea of a ductile deformation of the lower crust caused by a rapid return flow of metamorphic rocks that spread out below the forearc (Becker et al. 2010). In the region of the Pliny trench at the SE of Crete, a SE-dipping seismogenic structure is observed that combines with the seismicity of the Pliny trench at a depth from 15 to 40 km (Fig. 6). The Pliny trench east of Crete indicates a seismic activity during the observation period and seems to be deforming seismically.

Prominent crustal seismic activity within the AS plate in the area of eastern Crete is observed throughout the whole observation period (Figs. 6, 10). This activity close to the eastern coast of Crete and southern coast of the Kasos and Karpathos Islands was also identified in earlier seismicity studies of the region (Delibasis et al. 1999; Meier et al. 2004; Becker et al. 2006, 2010). Combining our findings with the ISC catalog (Engdahl et al. 1998), we conclude that

Fig. 6 Epicenters of the eastern Crete EQ sequence. The size of the epicenters is proportional to magnitude. Profiles labeled B–B', C–C' and D–D' represent directions of seismic cross sections. The colors of the hypocenters are related to the seismic profiles (i.e., B–B' red, C–C' orange and D–D' purple). Seismic cross section along B–B', C–C' and D–D' directions are shown at the bottom. The black dashed line indicates Moho depth along the study area (Meier et al. 2004; Becker et al. 2010)

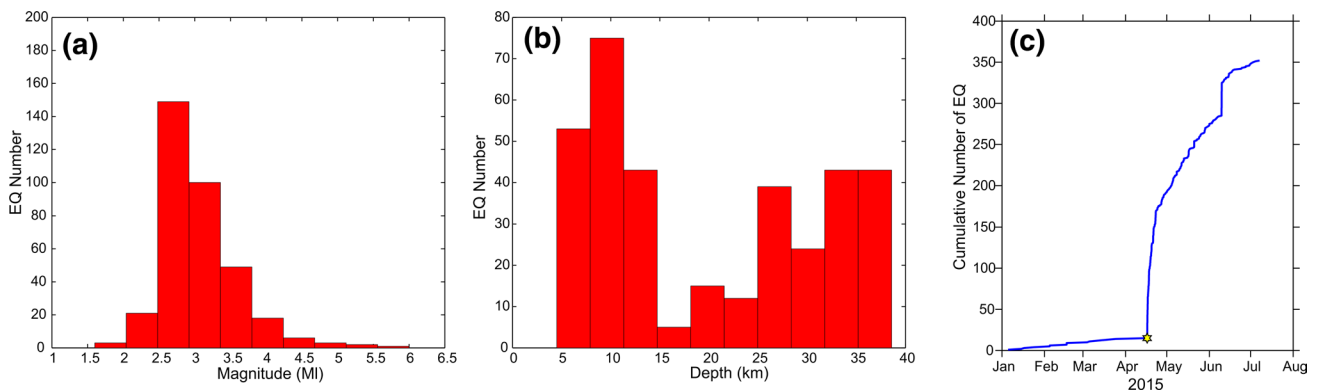
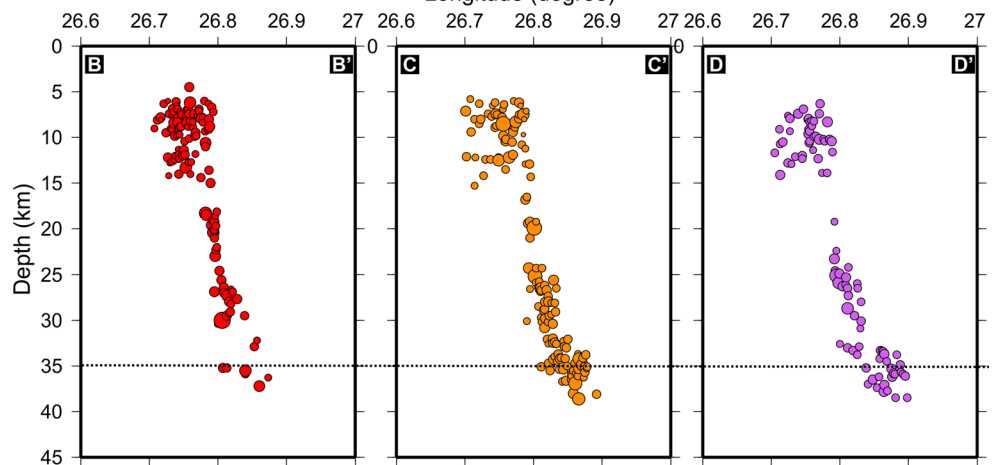
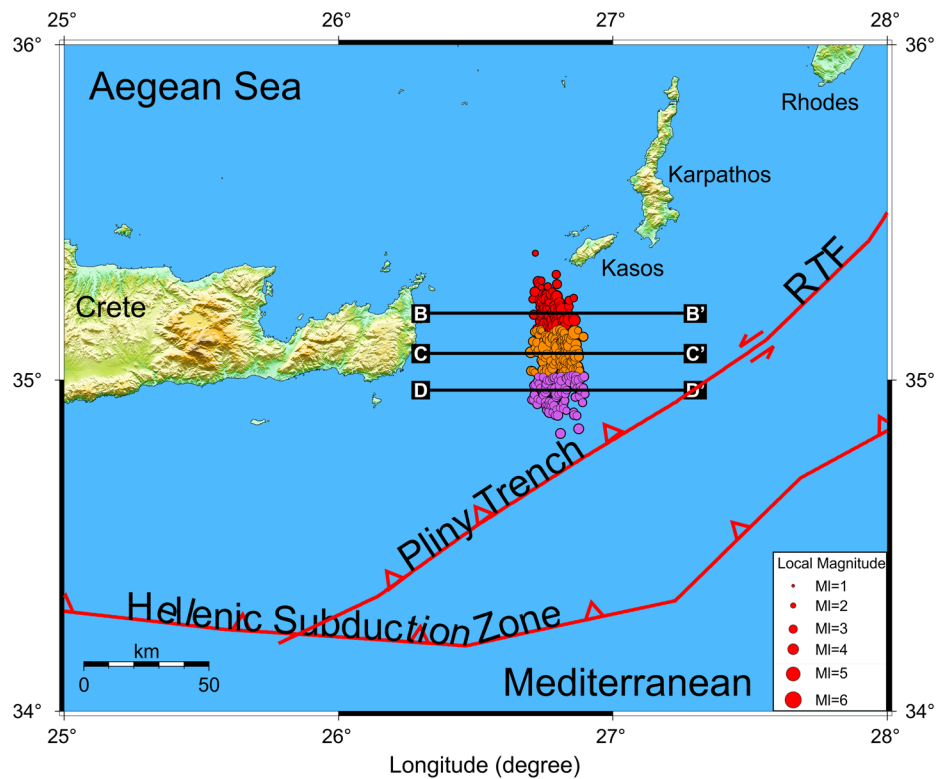


Fig. 7 Frequency of analyzed events with respect **a** to the computed MI and **b** to the computed hypocentral depth. Cumulative number of EQ for the entire catalog is shown in **c**. Yellow star indicates the mainshock

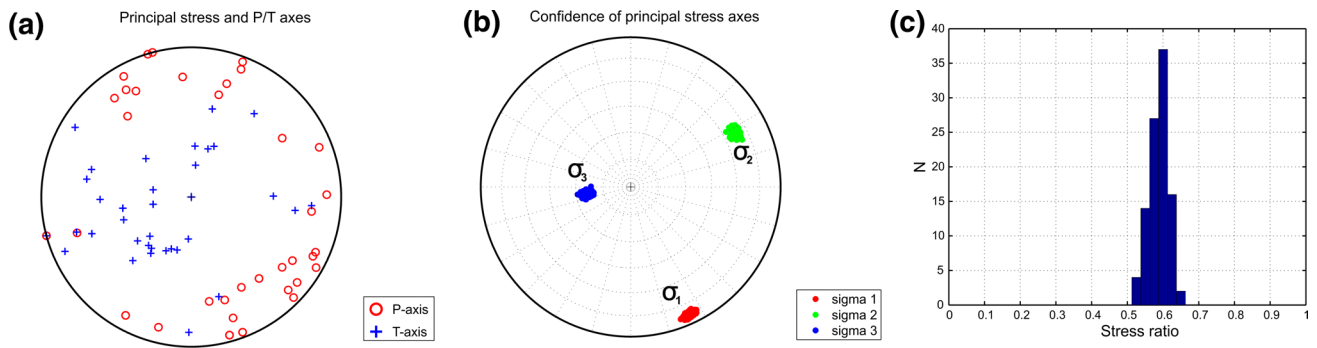


Fig. 8 **a** P and T axes for the events in Fig. 2 with retrieved principal stress directions. The P and T axes are marked by *red circles* and *blue plus signs*, respectively. **b** Confidence limits of the principal stress directions retrieved by the iterative method (Vavryčuk 2014). *Red, green* and *blue colors* correspond to the σ_1 , σ_2 and σ_3 stress

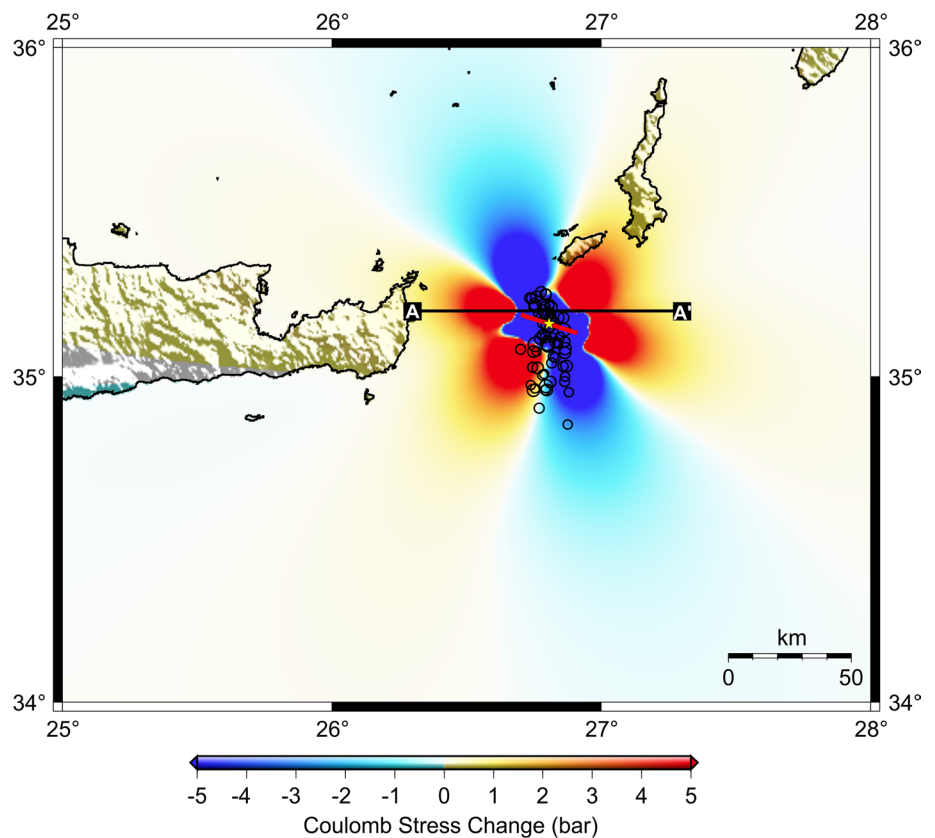
directions, respectively. The contours around the best model define the 95 % confidence region of each stress axis. **c** Histograms of the stress ratio (ϕ), which is found to be 0.60. This value indicates that the study region is described by transtensional stress regime

Table 2 Results of stress tensor inversion for the entire set of 45 focal mechanisms in the region offshore eastern Crete

Volume	No. Fps	σ_1 (Az)	σ_1 (Pl)	σ_2 (Az)	σ_2 (Pl)	σ_3 (Az)	σ_3 (Pl)	Misfit	R	Var.
OEC EQ	45	153	4	61	26	250	64	44	0.60	0.18

OEC EQ represents the events offshore eastern Crete. Results are based on all fault plane solutions (Fig. 2) OEC EQ represents the offshore eastern Crete earthquake. Results contain number of fault plane solutions within the relevant volume, directions for the three principal stresses (σ_{1-3}) in terms of azimuth and plunge, average misfit ($\bar{\beta}$), stress ratio (R) and variance

Fig. 9 Coulomb stress change, taking into account the 2015 eastern Crete mainshock. Color palette of Coulomb stress values is leveled in the range $-5/+5$ bar. *Red color* represents positive stress changes, while *blue negative*. *Yellow star* indicates the 16 April 2015 M_w 6.0 mainshock. *Red lines* display the coseismic rupture based on the calculated focal mechanisms. *Black circles* represent $M_I \geq 3.5$ aftershocks of the eastern Crete EQ from 16 April to 7 July 2015. *Yellow star* represents the mainshock



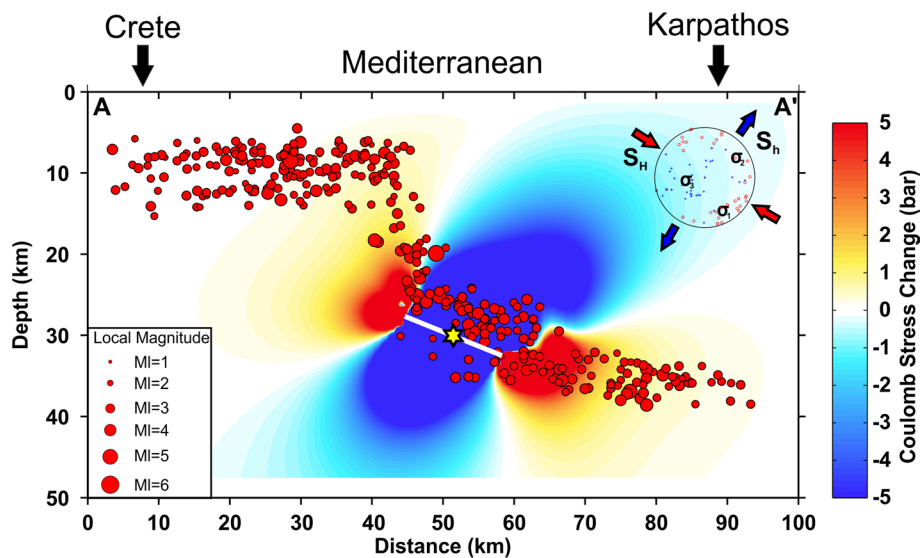


Fig. 10 A Cross section of 352 earthquake hypocenters along the subduction zone for A–A' profile shown in Fig. 9. White line donates the 16 April 2015 M_w 6.0 EQ coseismic rupture fault geometry based on this study (Table 1). Stress regime obtained in this study is represented by a solid white circle as a thrust regime. Red and blue arrows display the maximum horizontal compressive stress (S_H) and the min-

imum horizontal compressive stress (S_h) from the stress tensor inversion, respectively. This cross section indicates clearly a Benioff zone in the region offshore eastern Crete associated with 7 months seismic activity (red circles) within 90 km of A–A' profile marked in Fig. 9. The size of the solid red circles is proportional to magnitude

the eastern Crete region composes a continuously seismically active feature in the Aegean crust. This crustal activity expands from near-surface depths (~5 km) down to the presumed plate interface at approximately 40 km depth. It is traced by this study in N–S direction from offshore Crete in the east and possibly even further east toward the Karpathos Island. An active transtensional regime offshore eastern Crete resulting in forearc slices separated from the Cretan block due to internal deformation of the Aegean crust in this area (ten Veen and Kleinspehn 2003). The development of these slices is explained by the blocking of the further outward expansion of the AS plate boundary in western Crete due to the incipient collision with the AF plate and the simultaneous expansion of the Aegean crust by the stretching of Cretan–Rhodes forearc in the east caused by the still active slab rollback in this area (ten Veen and Kleinspehn 2003; Becker et al. 2010; Meier et al. 2004). Seismic studies indicate similar wedge-shaped sedimentary basins in the vicinity of the Pliny trench (Bohnhoff et al. 2001). Toward the south of the Pliny trench, Becker et al. (2010) observed a sharp drop of crustal seismicity within the overriding AS plate and seismicity is almost exclusively found at the presumed plate interface. This observation is supported by the interpretation of ten Veen and Kleinspehn (2003). The Strabo trench has a similar character as the Pliny trench but it cannot be finally resolved due to absence of high precision earthquake locations (Becker et al. 2006, 2010). The microseismicity located at crustal depth between the Pliny and Strabo trenches (Becker et al.

2010) agrees with event locations of intermediate magnitude seismicity of the ISC catalog. However, this observation indicates that the region between the Pliny and Strabo trenches displays strong internal deformation and cannot be interpreted as a further forearc sliver. These observations are in agreement with the results of swath bathymetry and seismic reflection profiles (Huguen et al. 2001), which observed faulted, locally uplifted basement blocks south of the Pliny trench. According to Huguen et al. (2001), this southernmost domain of the Cretan continental margin is disconnected from its northern part by the Pliny trench.

The strong aftershock activity indicating the seismogenic part of the plate contact between the AF and AS plates, which has its eastern termination above the Pliny trench, expands to the east of Crete over a width approximately 90 km (Fig. 10). The eastern part of the interplate seismicity is also observed by earlier temporary seismic networks (Becker et al. 2010; Meier et al. 2004), while these studies are not able to detect its eastern termination due to the lack of events during the observation period. We interpret that this interplate seismicity is vertically scattered, and Coulomb changes indicating possible areas of stress accumulation are detected. Seismic activity in this region is also found in the instrumental ISC catalog. The accretionary complex to the NW of the Pliny trench produces only microseismic activity (i.e., no large- or intermediate-size events). Also, the presumed plate contact between the AF and AS plates north of the Pliny trench exhibits active seismic behavior. Figure 10 depicts the activity in this region at

high spatial resolution; indications for a SE-dipping structure merging with the seismicity of the Pliny trench at a depth of 20 km can be found. Below this depth, the current merged activity can be traced down to the observed depth of the plate contact at 40 km. The observed seismicity distribution might indicate a connection between the Pliny and Strabo trenches. Aftershock activity observed offshore Crete is confined to the upper 40 km of the crust and does not reach down to depths of the lower continental crust. Furthermore, a roughly NS-trending structure adjacent to the east coast of Crete with hypocentral depths between 5 and 40 km is active during the observation period (Fig. 10). The activation of NS- and NE–SW-trending thrust faults is in good agreement with the current stress field in the region offshore eastern Crete (Fig. 8). Seismicity within the Aegean lithosphere below Crete is low at depths approximately 20 km (Fig. 6) pointing to rather ductile deformation of the overriding plate in contrast to brittle behavior at shallower depths. These observations are in good agreement with numerical modelings of rheological properties of the plate contact in the forearc (Gerya et al. 2002; Gerya and Stöckhert 2006; Becker et al. 2010). These modelings forecast rapid return flow of metamorphic rocks, including hydrated mantle material, along the hanging wall of the subducted slab that spread out beneath the forearc and ductile behavior of the plate contact and deeper parts of the overriding plate in the region of the forearc high.

The coseismic Coulomb stress changes are correlated with the distribution of aftershocks in cross-sectional view (Fig. 10). Considering the location of the OEC EQ sequence, the zone with the negative stress values can reveal the expected dimension of the epicentral area (approximately 70 km). Taking into account these observations, the dimension of the activated region can be explained on the basis of the Coulomb failure criterion because of stress transfer loading. Both the upper crust (depth ≤ 40 km) and the crust beneath the fault plane are brought closer to failure. Afterslip on the fault plane acts to reload the upper crust (Fig. 10). This type of thrust faults may tend to increase the failure stress in the upper crust coseismically, producing confined and low productive aftershock sequence.

Conclusions

We present results from the 16 April 2015 M_w 6.0 OEC EQ sequence. A seismically active zone is detected in the Aegean lithosphere along the east of Crete. We determine 45 CMT solutions that cover M_w range from 3.3 to 6.0 for the HSZ in the vicinity of eastern Crete. NE–SW extensional thrust faulting on eastern Crete is interpreted as along-arc extension. The striking direction of σ_3 in the

eastern Crete reflects the SE-directed retreat of the plate boundary.

In the area of Pliny trench southeast of Crete, high seismic activity is observed in a zone that extends from the interplate seismicity at approximately 40 km depth toward upper crust. Within this zone, cluster of hypocenters indicate southeast dipping zones in east of Crete that corresponds to the horst character of Crete. The seismogenic part of the plate contact has a width of approximately 90 km from the area of Pliny trench in the south to roughly the east coast of Crete in the north. The plate contact below Crete and north of Pliny trench exhibits seismic behavior and therefore seems to be seismically coupled. Seismic activity at the plate contact is rather distributed, and we observe locked zones and corresponding stress accumulations during observation period.

Seismic activity below Crete is mainly confined to the upper 20 km indicating a ductile behavior of the lower crust. In the area of the offshore eastern Crete, a SE-dipping seismogenic structure is identified, which combines with the seismicity of the Pliny trench at a depth of 20 km. The downdip location limit of the seismogenic zone along the plate contact below the east coast of Crete complies with the idea of a return flow metamorphic material. This material is assumed to flow along the hanging wall of the subducted slab spreading out beneath the forearc and producing the rapid uplift of Crete. We suggest that this region constitutes a forearc slice which moves as a rigid block accommodating relative motions along the transtensional structures of the Pliny trench.

Acknowledgments Authors thank all members of Kandilli Observatory and Earthquake Research Institute, Disaster and Emergency Management Presidency Earthquake Department and the Geoforschungszentrum Potsdam GEOFON, Seismological Network of Crete, National Observatory of Athens, Aristotle University of Thessaloniki Seismological and MEDNET for providing the continuous seismological data used in this study. The author is also grateful to Dr. Masaru Nakano for providing the waveform inversion code. We would like to thank Prof. Dr. Wolf-Christian Dullo (Editor in Chief), Prof. Dr. Tuncay Taymaz and one anonymous reviewer for their constructive comments and suggestions, which improved the manuscript. All figures are generated by Generic Mapping Tools (GMT) code developed by Wessel and Smith (1998).

References

- Barka AA, Reilinger R, Şaroğlu F, Şengör AMC (1997) The eastern Isparta angle, its importance in neotectonics of the eastern Mediterranean region. IESCA-1995 Proceedings, vol 1, 3–17
- Becker D, Meier T, Rische M, Bohnhoff M, Harjes H-P (2006) Spatio-temporal microseismicity clustering in the Cretan region. *Tectonophysics* 423:3–16
- Becker D, Meier T, Bohnhoff M, Harjes H-P (2010) Seismicity at the convergent plate boundary offshore Crete, Greece, observed by an amphibian network. *J Seismol* 14:369–392

- Benetatos C, Kiratzi A, Papazachos C, Karakaisis G (2004) Focal mechanisms of shallow and intermediate depth earthquakes along the Hellenic Arc. *J Geodyn* 37(2):253–296
- Bird P (2003) An updated digital model of plate boundaries. *Geochim Geophys Geosyst* 4(3):1027. doi:[10.1029/2001GC000252](https://doi.org/10.1029/2001GC000252)
- Bohnhoff M, Makris J, Stavrakakis G, Papanikolaou D (2001) Crustal investigation of the Hellenic subduction zone using wide aperture seismic data. *Tectonophysics* 343:239–262
- Bohnhoff M, Meier T, Harjes H-P (2005) Stress regime at the Hellenic Arc from focal mechanisms. *J Seismol* 9:341–366
- Bohnhoff M, Gresser H, Dresen G (2006) Strain partitioning and stress rotation at the North Anatolian Fault Zone from aftershock focal mechanisms of the 1999 Izmit Mw = 7.4 Earthquake. *Geophys J Int* 166:373–385
- Bott MHP (1959) The mechanics of oblique slip faulting. *Geol Mag* 96:109–117
- Bouchon M (1979) Discrete wave number representation of elastic wave fields in three-space dimensions. *J Geophys Res* 84:3609–3614
- Delibasis N, Ziazia M, Voulgaris N, Papadopoulos T, Stavrakakis G, Papanastassiou D, Drakatos G (1999) Microseismic activity and seismotectonics of the Heraklion area (central Crete Island, Greece). *Tectonophysics* 308:237–248
- Delph JR, Biryol CB, Beck SL, Zandt G (2015) Shear wave velocity structure of the Anatolian Plate: anomalously slow crust in southwestern Turkey. *Geophys J Int* 202:261–276. doi:[10.1093/gji/ggv141](https://doi.org/10.1093/gji/ggv141)
- Endrun B, Meier T, Bischoff M, Harjes H-P (2004) Lithospheric structure in the area of Crete constrained by receiver functions and dispersion analysis of Rayleigh phase velocities. *Geophys J Int* 158:592–608
- Engdahl ER, van der Hilst R, Buland R (1998) Global teleseismic earthquake relocation with improved travel times and procedures for depth determination. *Bull Seismol Soc Am* 88:722–743
- Fichtner A, Trampert J, Cupillard P, Saygin E, Taymaz T, Capdeville Y, Villaseñor A (2013a) Multi-scale full waveform inversion. *Geophys J Int* 194(1):534–556. doi:[10.1093/gji/ggt118](https://doi.org/10.1093/gji/ggt118)
- Fichtner A, Saygin E, Taymaz T, Cupillard P, Capdeville Y, Trampert J (2013b) The deep structure of the North Anatolian fault zone. *Earth Planet Sci Lett* 373:109–117. doi:[10.1016/j.epsl.2013.04.027](https://doi.org/10.1016/j.epsl.2013.04.027)
- Gephart JW, Forsyth DW (1984) An improved method for determining the regional stress tensor using earthquake focal mechanism data: application to the san Fernando earthquake sequence. *J Geophys Res* 89(B11):9305–9320
- Gerya TV, Stöckhert B (2006) 2-D numerical modeling of tectonic and metamorphic histories at active continental margins. *Int J Earth Sci* 95:250–274
- Gerya TV, Stöckhert B, Perchuk AL (2002) Exhumation of high-pressure metamorphic rocks in a subduction channel—a numerical simulation. *Tectonics* 21:6–1–6–19
- Görgün E, Bohnhoff M, Bulut F, Dresen G (2010) Seismotectonic settings of the Karadere-Düzce branch of the North Anatolian Fault Zone between the 1999 Izmit and Düzce ruptures from analysis of Izmit aftershock focal mechanisms. *Tectonophysics* 482:170–181
- Hardebeck JL, Hauksson E (2001) Stress orientations obtained from earthquake focal mechanisms: what are appropriate uncertainty estimates? *Bull Seismol Soc Am* 97:826–842
- Huguen C, Mascle J, Chaumillon E, Woodside JM, Benkhelil J, Kopf A, Volkonskaya A (2001) Deformation styles of the eastern Mediterranean Ridge and surroundings from combined swath mapping and seismic reflection profiling. *Tectonophysics* 343:21–47
- Jost M, Knabenbauer O, Cheng J, Harjes H-P (2002) Fault plane solutions of microearthquakes and small events in the Hellenic Arc. *Tectonophysics* 356:87–114
- Kind R, Eken T, Tilmann F, Sodoudi F, Taymaz T, Bulut F, Yuan X, Can B, Schneider F (2015) Thickness of the lithosphere beneath Turkey and surroundings from S-receiver functions. *Solid Earth* 6:971–984. doi:[10.5194/se-6-971-2015](https://doi.org/10.5194/se-6-971-2015)
- King GCP, Stein RS, Lin J (1994) Static stress changes and the triggering of earthquakes. *Bull Seismol Soc Am* 84:935–953
- Kiratzi A, Louvari E (2003) Focal mechanisms of shallow earthquakes in the Aegean Sea and the surrounding lands determined by waveform modelling: a new database. *J Geodyn* 36(1–2):251–274
- Knapmeyer M, Harjes H-P (2000) Imaging crustal discontinuities and the downgoing slab beneath western Crete. *Geophys J Int* 143:1–22
- Kreemer C, Chamot-Rooke N (2004) Contemporary kinematics of the southern Aegean and the Mediterranean Ridge. *Geophys J Int* 157:1377–1392
- Le Pichon X, Kreemer C (2010) The Miocene-to-Present Kinematic Evolution of the Eastern Mediterranean and Middle East and Its Implications for Dynamics. *Annu Rev Earth Planet Sci* 38:323–351
- Le Pichon X, Chamot-Rooke N, Lallemand S (1995) Geodetic determination of the kinematics of central Greece with respect to Europe: implications for eastern Mediterranean tectonics. *Geophys Res* 100:12675–12690
- Lienert BRE, Havskov J (1995) A computer program for locating earthquakes both locally and globally. *Seismol Res Lett* 66:26–36
- Lin J, Stein RS (2004) Stress triggering in thrust and subduction earthquakes, and stress interaction between the southern San Andreas and nearby thrust and strike-slip faults. *J Geophys Res* 109:B02303. doi:[10.1029/2003JB002607](https://doi.org/10.1029/2003JB002607)
- Lu Z, Wyss M, Pulpan H (1997) Details of stress directions in the Alaska subduction zone from fault plane solutions. *J Geophys Res* 102:5385–5402
- Lund B, Slunga R (1999) Stress tensor inversion using detailed micro-earthquake information and stability constraints: application to Olfus in southwest Iceland. *J Geophys Res* 104:14.947–14.964
- Mascle J, Le Cleach A, Jongsma D (1986) The eastern Hellenic margin from Crete to Rhodes: example of progressive collision. *Mar Geol* 73:145–168
- McCloskey J, Nalbant SS, Steacy S, Nostro C, Scotti O, Baumont D (2003) Structural constraints on the spatial distribution of aftershocks. *Geophys Res Lett* 30(12):1610. doi:[10.1029/2003GL017225](https://doi.org/10.1029/2003GL017225)
- McClusky B, Balassanian S, Barka A, Demir C, Ergintav S, Georgiev I, Gurkan O, Hamburger M, Hurst K, Kahle H, Kastens K, Kekelidze G, King R, Kotzev V, Lenk O, Mahmoud S, Mishin A, Nadariya M, Ouzounis A, Paradissis D, Peter Y, Prilepin M, Reilinger R, Sanli I, Seeger H, Tealeb A, Toksöz MN, Veis G (2000) Global positioning system constraints on plate kinematics and dynamics in the eastern Mediterranean and Caucasus. *J Geophys Res* 105:5695–5719
- McKenzie D (1978) Active Tectonics of the Alpine-Himalayan belt: the Aegean Sea and surrounding regions. *Geophys J Int* 55:217–254
- Meier T, Rische M, Endrun B, Vafidis A, Harjes H-P (2004) Seismicity of the Hellenic subduction zone in the area of western and central Crete observed by temporary local seismic networks. *Tectonophysics* 383:149–169
- Michael AJ (1984) Determination of stress from slip data: faults and folds. *J Geophys Res* 89:11517–11526
- Michael AJ (1987) Use of focal mechanisms to determine stress: a control study. *J Geophys Res* 92:357–368
- Michael AJ (1991) Spatial variations of stress within the 1987 Whittier Narrows, California, aftershock sequence: new techniques and results. *J Geophys Res* 96:6303–6319

- Michael AJ, Ellsworth WL, Oppenheimer D (1990) Co-seismic stress changes induced by the 1989 Loma Prieta, California earthquake. *Geophys Res Lett* 17:1441–1444
- Nakano M, Kumagai H, Inoue H (2008) Waveform inversion in the frequency domain for the simultaneous determination of earthquake source mechanism and moment function. *Geophys J Int* 173:1000–1011
- Nakano M, Yamashina T, Kumagai H, Inoue H, Sunarjo (2010) Centroid moment tensor catalogue for Indonesia. *Phys Earth Planet Inter* 183:456–467
- Nyst M, Thatcher W (2004) New constraints on the active tectonic deformation of the Aegean. *J Geophys Res* 109:B11406. doi:10.1029/2003JB002830
- Papazachos BC (1996) Large seismic faults in the Hellenic arc. *Ann Geofis* 39:891–903
- Papazachos BC, Karakostas VG, Papazachos CB, Scordilis EM (2000) The geometry of the Wadati–Benioff zone and lithospheric kinematics in the Hellenic Arc. *Tectonophysics* 319:275–300
- Reasenbergh PA, Simpson RW (1992) Response of regional seismicity to the static stress change produced by the Loma Prieta earthquake. *Science* 255:1687–1690. doi:10.1126/science.255.5052.1687
- Reilinger R, McClusky S, Vernant P, Lawrence S, Ergintav S, Cakmak R, Ozener H, Kadirov F, Guliev I, Stepanyan R, Nadariya M, Hahubia G, Mahmoud S, Sakr K, ArRajehi A, Paradissis D, Al-Aydrus A, Prilepin M, Guseva T, Evren E, Dmitrova A, Filikov SV, Gomez F, Al-Ghazzi R, Karam G (2006) GPS constraints on continental deformation in the Africa–Arabia–Eurasia continental collision zone and implications for the dynamics of plate interactions. *J Geophys Res* 111:B05411. doi:10.1029/2005JB004051
- Reilinger R, McClusky S, Paradissis D, Ergintav S, Vernant P (2010) Geodetic constraints on the tectonic evolution of the Aegean region and strain accumulation along the Hellenic subduction zone. *Tectonophysics* 488:22–30
- Roumelioti Z, Kiratzi A, Benetatos C (2011) Time-Domain Moment Tensors for shallow ($h \leq 40$ km) earthquakes in the broader Aegean Sea for the years 2006 and 2007: the database of the Aristotle University of Thessaloniki. *J Geodyn* 51:179–189
- Saltogrianni V, Gianniu M, Taymaz T, Yolsal-Çevikbilen S, Stiros S (2015) Fault-Slip Source Models for the 2014 Mw 6.9 Samothraki-Gökçeada Earthquake (North Aegean Trough): combining geodetic and seismological observations. *J Geophys Res (JGR) Solid Earth*. doi:10.1002/2015JB012052
- Şaroğlu F, Emre Ö, Kuşcu İ (1992) Active Fault Map of Turkey, General Directorate of Mineral Research and Exploration (MTA), Eskisehir Yolu, 06520, Ankara, Turkey
- Şengör AMC, Görür N, Şaroğlu F (1985) Strike-slip faulting and related basin formation in zones of tectonic escape: Turkey as a case study. *Society of Economic Paleontologists and Mineralogists*. Special Publication, vol 37, pp 227–264
- Shaw B, Jackson J (2010) Earthquake mechanisms and active tectonics of the Hellenic subduction zone. *Geophys J Int* 181:966–984
- Skarlatoudis AA, Papazachos CB, Margaritis BN, Papaioannou C, Ventouzi C, Vamvakaris D, Bruestle A, Meier T, Friederich W, Stavrakakis G, Taymaz T, Kind R, Vafidis A, Dahm T (2009) Combination of acceleration-sensor and broadband velocity-sensor recordings for attenuation studies: the case of the 8 January 2006 Kythera Intermediate-Depth Earthquake. *Bull Seismol Soc Am* 99(2A):694–704. doi:10.1785/0120070211
- Soudou F, Kind R, Hatzfeld D, Priestly K, Hanka W, Wylegalla K, Stavrakakis G, Vafidis A, Harjes H-P, Bohnhoff M (2006) Lithospheric structure of the Aegean obtained from P and S receiver functions. *J Geophys Res* 111:B12307. doi:10.1029/2005JB003932
- Taymaz T, Price S (1992) The 1971 May 12 Burdur Earthquake sequence, SW Turkey: a synthesis of seismological and geological observations. *Geophys J Int* 108:589–603
- Taymaz T, Jackson J, Westaway R (1990) Earthquake mechanisms in the Hellenic Trench near Crete. *Geophys J Int* 102:695–731
- Taymaz T, Jackson JA, McKenzie D (1991) Active tectonics of the north and central Aegean Sea. *Geophys J Int* 106:433–490
- ten Veen JH, Kleinspehn KL (2003) Incipient continental collision and plate-boundary curvature: late Pliocene–Holocene transtensional Hellenic forearc, Crete, Greece. *J Geol Soc* 160:161–181
- Toda S, Stein RS, Richards-Dinger K, Bozkurt S (2005) Forecasting the evolution of seismicity in southern California: animations built on earthquake stress transfer. *J Geophys Res* 110:B05S16. doi:10.1029/2004JB003415
- Toda S, Lin J, Meghraoui M, Stein RS (2008) 12 May 2008 M = 7.9 Wenchuan, China, earthquake calculated to increase failure stress and seismicity rate on three major fault systems. *Geophys Res Lett* 35:L17305. doi:10.1029/2008GL034903
- Toda S, Stein RS, Lin J (2011) Widespread seismicity excitation throughout central Japan following the 2011 M = 9.0 Tohoku earthquake and its interpretation by Coulomb stress transfer. *Geophys Res Lett* 38:L00G03. doi:10.1029/2011GL047834
- Vanacore EA, Taymaz T, Saygin E (2013) Moho structure of the Anatolian Plate from receiver function analysis. *Geophys J Int* 193(1):329–337. doi:10.1093/gji/ggs107
- Vavryčuk V (2014) Iterative joint inversion for stress and fault orientations from focal mechanisms. *Geophys J Int* 199:69–77. doi:10.1093/gji/ggu224
- Waldhauser F, Ellsworth WL (2000) A double-difference earthquake location algorithm: method and application to the Northern Hayward fault, California. *Bull Seismol Soc Am* 90:1353–1368
- Wallace RE (1951) Geometry of shearing stress and relationship to faulting. *J Geol* 59:118–130
- Wessel P, Smith WHF (1998) New, improved version of the Generic Mapping Tools Released. *EOS Trans., American Geophysical Union*, 79, 579
- Wiemer S, Gerstenberger MC, Hauksson E (2002) Properties of the 1999, Mw 7.1, Hector Mine earthquake: implications for after-shock hazard. *Bull Seismol Soc Am* 92:1227–1240
- Yolsal-Çevikbilen S, Taymaz T (2012) Earthquake source parameters along the Hellenic subduction zone and numerical simulations of historical Tsunamis in the Eastern Mediterranean. *Tectonophysics* 536–537:61–100. doi:10.1016/j.tecto.2012.02.019
- Yolsal-Çevikbilen S, Taymaz T, Helvacı C (2014) Earthquake mechanisms in the Gulfs of Gökova, Sığacık, Kuşadası, and the Simav Region (western Turkey): neotectonics, seismotectonics and geodynamic implications. *Tectonophysics* 635:100–124. doi:10.1016/j.tecto.2014.05.001
- Zang A, Stephansson O (2010) *Stress field of the Earth's crust*. Springer, Dordrecht
- Zoback ML (1992) First and second order patterns of stress in the lithosphere: the world stress map project. *J Geophys Res* 97:11703–11728